Materials Advances

ROYAL SOCIETY OF CHEMISTRY

PAPER

View Article Online
View Journal | View Issue

Cite this: *Mater. Adv.*, 2021, **2**, 1752

Disparity in piezofluorochromism for twisted mono-carbazole-based AIEgens resulting from interchanging electron-rich substituents: effect of coplanarity on twisted π-conjugates†

Banchhanidhi Prusti and Manab Chakravarty *

Carbazole-based aggregation-induced emission-active fluorogens (AIEgens) with piezo-fluorochromic (PFC) features have enhanced the scope of a wide variety of applications in the field of optical recording and security displays. However, ambiguity resulting from the various research outcomes motivates researchers to find a smart strategy that can generate a significant number of PFC-active materials. This article reports the design of mono-carbazole (**CBZ**)-linked unsymmetrically decorated anthracenyl π-conjugates **TMBπCBZ** (Φ_F = 61%) and **CBZπTMB** (Φ_F = 43%) [π = anthracene-linked vinyl] as AIEgens and strong solid-state emitters. The electron-rich trimethoxybenzene (**TMB**) unit is introduced within this **CBZ**-linked anthracenyl π-conjugated system and the strategy of interchanging **TMB** and **CBZ** affords two small organic positional isomers in an inexpensive and easily accessible route. Interestingly, after grinding in a mortar and pestle or quick pressing (in an infrared pellet maker: 20 MPa), **TMBπCBZ** displays reversible spectacular PFC features with a 62 nm redshift, whereas **CBZπTMB** remains unchanged. Thus, the interchange between the **TMB** and **CBZ** units in the same scaffold results in notable PFC-behavior and establishes a novel structure–property relationship. A single crystal study disclosed the difference in the molecular twisting and packing in the solid-state for these isomers. A powerful intramolecular interaction (2.15 Å) between –OMe and olefinic-CH (π) in **CBZπTMB** imposes greater coplanarity to the system and achieves a relatively stable conformation, whereas **TMBπCBZ** attains a more twisted molecular conformation, and a large number of weak intermolecular interactions (mainly C···H, no π···π) with cavities within the crystal motif induce the PFC-activity. Thus, a novel concept is reported, the coplanarity effect in these twisted systems appears to be unfavorable for the exhibition of PFC-features in these AIEgens. This fact is further supported by the results of the powder X-ray diffractometry, differential scanning calorimetry, and lifetime measurement studies. In addition, the intermolecular interactions were quantified using Hirshfeld-surface analyses, which substantiated the observed facts. Finally, **TMB-An-π-CBZ** is recognized as a promising platform for rewritable optical-recording and security-based applications.

Received 28th November 2020,
Accepted 8th February 2021

DOI: 10.1039/d0ma00933d

rsc.li/materials-advances

Introduction

The molecular response of changing photoluminescence (PL) properties as a result of various stimuli conveys the fundamental basis of PL switching, security papers, optoelectronic devices, and data storage in several applied fields.[1–5] An observable color change from the same molecule, without any tedious chemical modifications, offers significant benefits. However, this emission color change under mechanical force/pressure in the solid-state is difficult to predict or design. The PL property depends on the HOMO (highest occupied molecular orbital)–LUMO (lowest unoccupied molecular orbital) energy levels that alter owing to different molecular arrangements, intermolecular interactions, and conformational flexibility.[6] Although various molecular systems have been studied that show piezo-fluorochromic (PFC)-features, it appears to be quite challenging to fabricate materials with PFC-features. Each identified design is expressed as a unique system.[7] The main drawbacks include solid-state emission from small organic molecules owing to the aggregation-caused quenching (ACQ) effect and the lack of an appropriate strategy to generate PFC-active materials.[8] In this context, unique optical properties, thermal stability, richness in

Department of Chemistry, BITS-Pilani Hyderabad Campus, Jawahar Nagar, Shameerpet, Hyderabad-500078, Telangana, India
E-mail: manab@hyderabad.bits-pilani.ac.in

† Electronic supplementary information (ESI) available. CCDC 2043011 and 2043012. For ESI and crystallographic data in CIF or other electronic format see DOI: 10.1039/d0ma00933d

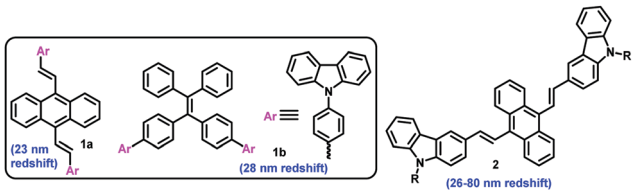

Fig. 1 Known symmetrically substituted bis-carbazole-based PFC-active compounds.

molecular modifications, and strong hole-transporting abilities in the optoelectronic devices have resulted in the carbazole unit being a promising candidate for attachment to various twisted π-conjugates to exhibit aggregation-induced emission (AIE) and PFC-features.[9a–f] Carbazole-based D–π–A systems[11a,b,10] and dendrons with multiple carbazole units have been judiciously designed, but only a few of them display a marginal PFC behavior.[12] Difficulties in switching from the crystalline to the amorphous state under pressure result in a barrier. The polymeric material embedded with carbazole offered mechano-fluorochromic (MFC) properties, but the elusive and complicated molecular structure of the polymeric material is a disadvantage.[13] The reported symmetrically substituted bis-carbazole-based anthracenyl π-conjugate **1a** (Fig. 1) displayed a redshift of 24 nm, and a further π-extension with six carbazole units gave a redshift of only 32 nm.[14] Another symmetrical analog, **2** was relatively more impressive, with a redshift range of 26–80 nm depending on the *N*-alkyl chain length.[15] The carbazole units were then added to traditional tetraphenyl AIEgens (**1b**); however, the PFC-property was not prominent.[16] Thus, the ACQ-effect, lack of generalization, and ill-defined path create a considerable challenge to the development of solid-state emitters with PFC-features. However, these materials offer a high demand for security-based technological development. The earlier reports on positional isomer-based organic molecules are rarely associated with a significant difference in the PFC-features.[24]

By keeping these concerns in mind, and based on our previous work on π-conjugates as AIEgens,[17] we herein report relatively small mono-carbazole and trimethoxybenzene-linked unsymmetrically substituted anthracenyl π-conjugates **CBZπTMB** and **TMBπCBZ** (Fig. 2) as AIEgens, in which the electron-rich **CBZ** and **TMB** are interchanged within the core. This interchange strategy reveals a novel structure–property relationship

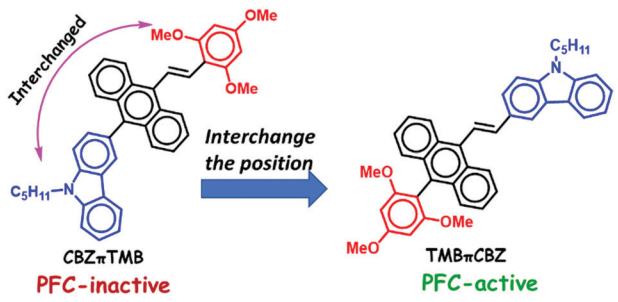

Fig. 2 The positional isomeric molecules reported herein.

in the PFC-active materials, in which the coplanarity effect on a twisted system becomes harmful to the PFC-features. Hence, the difference in PFC for these two positional isomers **TMBπCBZ** and **CBZπTMB** is demonstrated using various experimental and theoretical methods. Excitingly, both the molecules have a twisted conformation and show an enhanced emission in the aggregated state. Still, the PFC-feature is only observed for **TMBπCBZ**, which is established as an encouraging candidate for optical recording.

Results and discussion

(i) Synthesis and characterization

Owing to the crucial role of **TMB** in initiating a variety of supramolecular interactions[18] and **CBZ** as a PFC-enhancing core,[9] the combination of **TMB** and **C5-CBZ** is preferred. The designed compounds **CBZπTMB** and **TMBπCBZ** were easily synthesized in high yields (~80%) using simple, inexpensive Horner–Wadsworth–Emmons reactions at room temperature from easily accessible phosphonates and aldehydes (Scheme S1, ESI†). Thus, an expensive metal/ligand combination is completely avoided to access these molecules in which the **TMB** and **CBZ** units are introduced *via* the Friedel–Crafts arylation reaction. We could scale up this reaction on the gram scale, indicating easy access to these materials for real-world applications. The compounds were well characterized using multinuclear NMR, infrared spectroscopy (IR), and mass spectrometry studies. Finally, the molecular structure, with an (*E*)-configuration, was unambiguously confirmed using single-crystal X-ray diffraction studies (SCXRD). The presence of the carbazole unit raises the thermal stability of the π-conjugates[19] and the stability is maintained up to 350 °C and beyond (450 °C) as confirmed using thermogravimetric analysis (TGA, Fig. S1, ESI†).

(ii) AIE-studies

Having a twisted conformation, AIEgens are typically solid-state emitters with PFC features, and hence the AIE-properties of these molecules were studied. The photophysical behavior was systematically explored in both the solution and solid-state for these π-conjugates. A sharp maximum absorption at an λ_{abs} of approximately 405 nm was noticed for both the isomers in the absorption spectra (Fig. S2, ESI†) whereas a faint emission maximum at λ_{em} = 504 nm was observed for **CBZπTMB** and at 518 nm for **TMBπCBZ** in the PL spectra (Fig. S2, ESI†), indicating the slightly better π-electronic conjugation for **TMBπCBZ** in the solution state. There was almost no solvatofluorochromic effect observed (Fig. S2, ESI†), possibly owing to the deficit of polarity within this molecule in the solution state. In acetonitrile, **CBZπTMB** was almost non-emissive, and **TMBπCBZ** emits relatively better. The AIE-properties were inspected by measuring the absorption (Fig. S3, ESI†) and emission spectra (Fig. 3) for each compound in 10 μM acetonitrile solution upon the gradual addition of a water fraction (a nonsolvent f_w (v/v%)). The enhancement of the PL intensity was observed for both cases with a negligible variation in the emission wavelength. Still, the

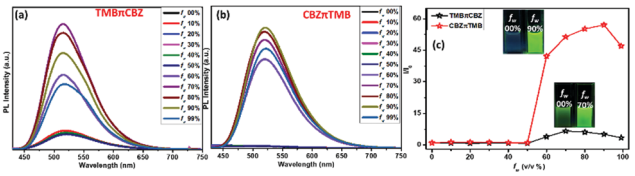

Fig. 3 Emission spectra of (a) **TMBπCBZ**, and (b) **CBZπTMB**. (c) The I/I_0 plot (I_0: Fl. intensity before the addition of water; I: Fl. intensity after the addition of water). Concentration of the probe: 10 μM, λ_{ex} = 405 nm. The image was taken at f_w = 0% and f_w = 90% (**CBZπTMB**) and 70% (**TMBπCBZ**) under 365 nm UV light at different f_w values in acetonitrile.

AIE-effect is more prominent for **CBZπTMB** (60 times enhancement), while **TMBπCBZ** displayed the AEE-effect (aggregation-enhanced emission) and the PL was boosted 15 times (Fig. 3c). The aggregation at the highest PL intensity was confirmed by the average size of the particles calculated using dynamic light scattering (DLS) studies, revealing 240 nm for **TMBπCBZ** and 177 nm for **CBZπTMB** (Fig. S4, ESI†). Based on Prof. Tang's extensive work on AIEgens, the restricted intramolecular motion is the primary cause for these twisted molecules.[20a–c] The smaller particle size may favor the greater AIE-effect for **CBZπTMB**.[21] However, we emphasized the photophysical behavior, mostly in the solid-state, to investigate the PFC-features.

(iii) PFC-studies

The solid-state photophysical properties were initially studied before and after grinding the pristine samples of the positional isomers to check the emission change. The solid-state UV-vis spectrum shows a broad and significant absorption in the region of 420–430 nm, mainly due to the π–π* transition along with a small signature at 690 nm (possibly a charge-transfer) for both the pristine samples. After grinding in a mortar and pestle, or by applying pressure (20 MPa) using an IR-pellet maker, the absorption spectrum is slightly redshifted (~20 nm) for **TMBπCBZ**, but no change was observed for **CBZπTMB** (Fig. S5, ESI†). However, the solid-state PL spectrum for **TMBπCBZ** is significantly redshifted from 520 to 582 nm after grinding. The absolute quantum yield (Φ_F) for the pristine sample was 61%, and this reduced to only 52% after grinding. Thus, one can visualize the sharp changes from a green to an orange emitting solid (62 nm contrast) using the naked eye under a 365 nm UV lamp after grinding the solid. Upon exposure of the orange solid to dichloromethane (DCM), it reverts back to the original green color. This repeated fluorescence switching is almost equal even after multiple grinding/fuming (Fig. S6, ESI†) processes. Notably, thermal energy could not bring back the original green color. This reversible color change upon numerous cycles of solvent exposure is highly impressive, but it was only exhibited by **TMBπCBZ**. On the other hand, the isomer **CBZπTMB** emits a strong yellow light (λ_{em} = 554 nm) with Φ_F = 43% and remains unaffected upon grinding (Fig. 4).

Additionally, the fluorescence lifetime of the excited state was measured for the solid **CBZπTMB** and **TMBπCBZ** in both the pristine and ground states (Fig. S7 and Table S1, ESI†). The fluorescence lifetime (τ/ns) is considerably larger for **TMBπCBZ** (4.05) than for

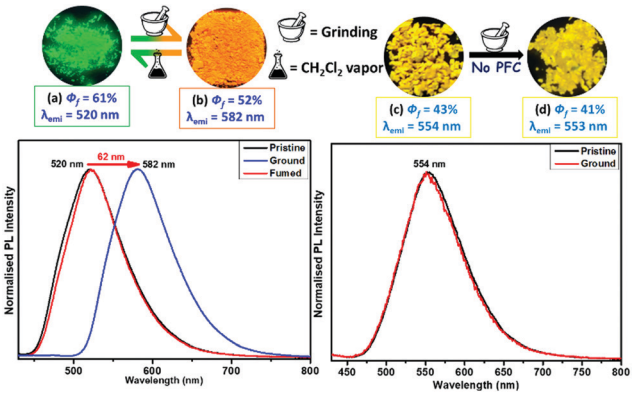

Fig. 4 (a) Pristine sample and (b) ground sample of **TMBπCBZ** and the corresponding reversible emission spectra λ_{ex} = 420 nm. (c) Pristine sample and (d) ground sample of **CBZπTMB** and the unchanged emission spectra λ_{ex} = 430 nm. The images were taken under a 365 nm UV lamp. (e) The reversibility up to six cycles.

Table 1 Parameters related to the solid-state fluorescence measurements

Samples	States	λ_{em}^{max} (nm)	Φ_f (%)	τ (ns)
TMBπCBZ	Pristine	520	61	4.05
	Ground	582	52	2.36
CBZπTMB	Pristine	554	43	2.21
	Ground	553	41	1.50

CBZπTMB (2.21) and thus supports a relatively higher Φ_F (%) as stated in Table 1. After grinding the compounds, the lifetime is reduced (Table 1) for both of them, resulting in a decrease in the quantum yield.

SCXRD studies. To give an insight into the above described variation in the PFC-features, both SCXRD and powder X-ray diffraction (PXRD) studies were performed. More importantly, the molecular structures determined from SCXRD revealed the fundamental difference between these two molecules in the solid-state (Fig. 5). The crystal parameters are tabulated in Table S2 (ESI†).

Both the structures are significantly twisted in the solid-state and hence emit efficiently through a radiative path to afford a

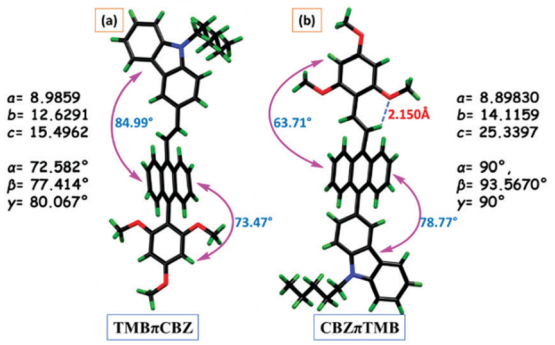

Fig. 5 Single-crystal X-ray structures and their twisting angles for (a) **TMBπCBZ** and (b) **CBZπTMB**.

Table 2 intermolecular interactions for both the π-conjugates

Compounds	C···H (Å)	O···H (Å)	H···H (Å)
TMBπCBZ (22 interactions)	2.844, 2.886, 2.837, 2.897, 2.870, 2.761, 2.823, 2.860, 2.820, 2.874, 2.845, 2.894, 2.839, 2.804, 2.783 (fifteen total)	2.588, 2.570, 2.619 (three)	2.368, 2.243, 2.306, 2.306 (four)
CBZπTMB (14 interactions)	2.891, 2.813, 2.833, 2.812, 2.869, 2.894, 2.876, 2.889, 2.891 (nine)	2.613 (one)	2.343, 2.373, 3.376, 2.190 (four)

high Φ_F. Direct attachment of the **TMB** unit with anthracene for **TMBπCBZ** causes a torsion angle of 73.5°, a little lower than the torsion angle with the **CBZ** unit (78.8°), resulting in a relatively better conjugation of **TMB** with anthracene. The remarkable planarity at the olefinic π-conjugated part (torsion angle: 63.7°) is achieved for **CBZπTMB** through a strong intramolecular interaction (2.15 Å) between –OMe and olefinic-H, forming a considerably stable six-membered ring, as presented in Fig. 5b. This interchange also affects the unit cell of the single crystal that governs **TMBπCBZ** in the triclinic ($P1$) and **CBZπTMB** in the monoclinic ($P21/c$) system.

Furthermore, a detailed inspection of the supramolecular interactions and modes of molecular crystal packing for **TMBπCBZ** and **CBZπTMB** offers an in-depth comparison to understand the switching of the solid-state fluorescence behavior upon grinding.[22,23] The intermolecular interactions for these crystals are described in Table 2 and Fig. 6. There are many interactions (22) for **TMBπCBZ** compared to **CBZπTMB** (14) owing to the presence of various types of CH and OMe substituents. However, no π···π interactions are observed because of these twisted conformations.

Notably, fifteen C···H interactions for **TMBπCBZ** impose a greater flexibility and are more likely to exhibit piezofluorochromism than the other isomer (*vide infra*).[24,25a] The packing of **TMBπCBZ** discloses a two-dimensional square motif with numerous weak C···H interactions (Fig. 7a and b). Furthermore, this packing also creates cavities that can provide flexibility to the system for conformational changes, possibly generated upon grinding. On the other hand, **CBZπTMB** is packed differently (V-type; Fig. 7c and d) with relatively fewer weak intermolecular interactions (C···H, Table 2). There was no sufficient void space observed as compared to **TMBπCBZ**. Thus, a significantly larger number of weak C···H interactions and the available cavities may result in a lower crystal lattice energy[25b] and facilitate **TMBπCBZ** to display PFC-features compared to **CBZπTMB**. This crystal packing with relatively loose interfaces between the layers can offer distortion under grinding/pressure by improving the degree of planarization in the molecular conformation that causes the observed redshift.[25c] The permeation of solvent vapor into the distorted crystal motif will allow molecules to become flexible and rearrange the molecular conformation to restore the pristine crystal packing to induce the actual emission.

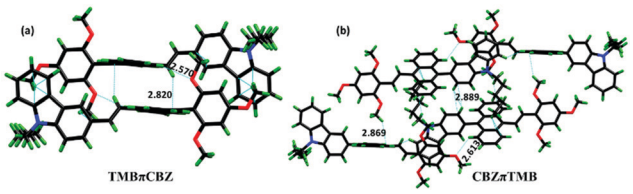

Fig. 6 Crystal packing for (a) **TMBπCBZ** and (b) **CBZπTMB** showing a few intermolecular interactions (d/Å).

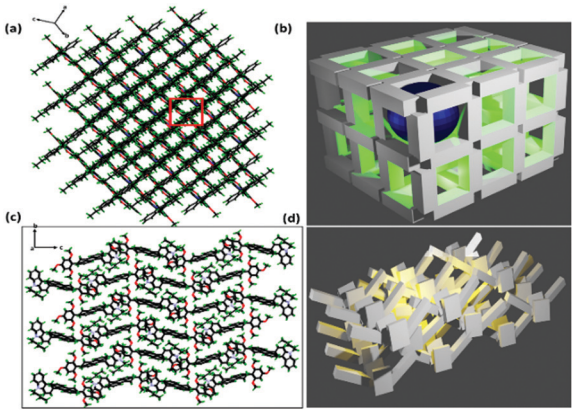

Fig. 7 Packing motif of (a) **TMBπCBZ**, (b) model with void space (blue sphere), (c) **CBZπTMB**, and (d) a representative diagram of this pattern.

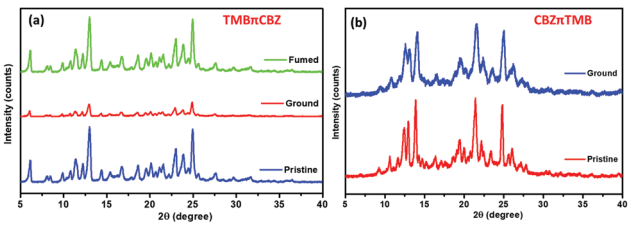

Fig. 8 The PXRD pattern of (a) **TMBπCBZ** after grinding and fuming, and (b) **CBZπTMB** (an unchanged diffractogram after grinding).

PXRD and DSC analysis. The disparity in PFC features between these two positional isomers is further elucidated by PXRD studies that show an entirely different diffractogram, as presented in Fig. 8, as expected owing to the other crystal structures. However, the reversible PFC behavior for **TMBπCBZ** is supported by the diffractogram for pristine, ground, and fumed samples. The pristine sample displays many sharp and intense diffraction signals, indicating a well-ordered crystalline structure. The transformation into a completely amorphous state was not observed for **TMBπCBZ** after grinding because low intense diffraction peaks at the same 2θ are observed. The original intense diffractions reappear upon fuming with DCM. This depicts a considerable decrease in the crystallinity (transformation towards the amorphous phase) after grinding the solid and restoring the crystallinity after fuming. Fuming with DCM facilitates the rearrangement of the molecules to

achieve the original crystalline state from the meta-stable phase. Surprisingly, crystalline **CBZπTMB** shows no change (Fig. 8b) in the diffractogram upon grinding owing to its relatively stable conformation with significant coplanarity. Thus, PXRD studies support this difference in the displaying of PFC-features for this phase transition in **TMBπCBZ**.

The PFC features of **TMBπCBZ** are further supported by the results of the DSC experiment, which were performed to gain a deeper insight into the changing emission color upon grinding. The DSC thermogram of both the pristine and ground solids were verified, the ground sample clearly indicates a difference with an extra exothermic cold crystallization peak at 82 °C, apart from the original signals (for the pristine sample) owing to melting (T_m) at 170 °C and vaporization (T_v) at 125 °C (Fig. S8, ESI†). The signal that represents T_v could originate from the adventitious solvent. This observation specifies that the crystalline state is not intact after grinding. This change in the crystal phase (a meta-stable phase) is responsible for the fluorescence switching upon grinding.[26–29,30a]

DFT studies and Hirshfeld surface analysis. Using the crystal information files (cif), the theoretical ground-state geometry and electronic structure of the molecules were optimized using density functional theory (DFT) with the B3LYP hybrid functional 6-31g(d,p) (Fig. S9, ESI†). The electronic structure of **CBZπTMB** reveals the HOMO is confined on the **CBZ**-linked anthracene core, and the LUMO is on the central anthracene. For **TMBπCBZ**, a similar distribution is observed as the HOMO is localized on the **TMB**-linked anthracene core, and the LUMO is on the anthracene. Thus, the HOMO is primarily built by the anthracene-attached electron-rich substituents, and the LUMO results from the anthracene.

Furthermore, the quantitative analysis of intermolecular interactions and void spaces are calculated through the Hirshfeld surface analysis (Fig. S10, ESI†). A significant amount of C···H type interactions (31.7%) act on the **TMBπCBZ** crystal compared to **CBZπTMB** (27.4%). Notably, there are no C···C interactions for **TMBπCBZ**, whereas **CBZπTMB** shows 3.4% of such interactions. The overall interactions are compared in the form of a histogram, as presented in Fig. 9a and b. The higher ratios of the C···H/C···C interactions indicate the good

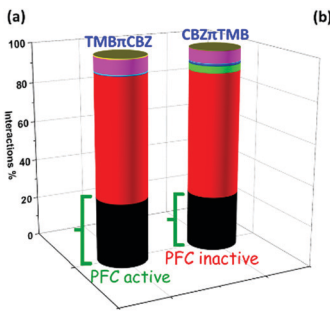

(b)

Interactions (%)	TMBπCBZ	CBZπTMB
C--H	31.7	27.4
H--H	60.3	61.8
C--C	0	3.4
C--O	0.2	0.9
N--H	0.5	0.3
O--H	6.8	5.8
O--O	0.5	0
C--N	0	0.4

Fig. 9 (a) Histogram offering all possible interactions and (b) quantitative interactions. Initially, the d_{norm} surface was generated with cif files in Crystal Explorer, and from there, all possible interactions were calculated through 2D finger plots (Fig. S10, ESI†).

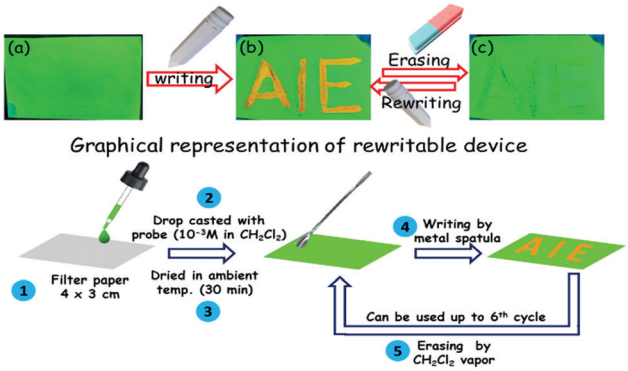

Fig. 10 Application of **TMBπCBZ** as a rewritable optical recorder.

PFC behavior for **TMBπCBZ**.[30b] The calculated void space is substantially higher for **TMBπCBZ** (624.4 Å^3) compared with **CBZπTMB** (328.5 Å^3) (Fig. S11, ESI†). This Hirshfeld analysis is very well aligned with the experimentally observed features and the crystal packing analysis. Thus, the difference in the intermolecular interactions and void space between these two molecules brings about an alteration in the PFC-features.

Application as an optical rewritable recorder. The application of these PFC-active materials was also demonstrated as a platform for rewritable optical recording. This high contrast fluorescence switching is very appropriate for applications. An inexpensive filter paper-based rewritable visual recorder was devised by drop-casting of a dilute (10^{-3} M) DCM solution of **TMBπCBZ**. After drying the filter paper at ambient temperature for 30 min, the yellow-emitting filter paper was ready for use. Anything can be conveniently written/drawn on this probe-coated filter paper, preferably using a metal spatula. The letters/drawing will appear yellow and visible by the naked eye under illumination from a 365 nm UV-torch (Fig. 10). The yellow emitting part can be further transformed into a green-emitting solid by fuming with DCM. Thus, this **TMBπCBZ**-coated filter paper is established as a promising PFC material for repeated use in optical recording and DCM can be used as a remover.

Experimental

Materials

All of the chemicals were purchased from Merck, and the solvents for column chromatography were purchased from Finar. Spectroscopic grade solvents used for UV-vis and fluorescence spectroscopy were obtained from Sisco Research Laboratories (SRL). All the experiments were performed at room temperature (298 ± 2 K). The ^{1}H and ^{13}C NMR spectra were recorded on Bruker 400 MHz spectrometers with operating frequencies of 101 MHz for ^{13}C. Chemical shifts (δ) are reported in ppm, relative to the residual solvent signal (δ 7.26 for ^{1}H NMR and δ 77.0 for ^{13}C NMR).

Methods and measurements

Steady-state absorption and fluorescence measurements. The solution-state absorption spectra were measured on a UV-vis-NIR spectrophotometer (Hitachi F7000, Japan), and

solid-state absorption spectra were recorded on a JASCO-500 spectrophotometer. The solid-state emission spectra were recorded using a fluorimeter (Fluorolog, HORIBA) and for the solution-state (FP-6300, Jasco) using a 10 mm path length quartz cuvette. All the solution-state spectra were recorded by maintaining the probe concentrations as 10 μM (2 mL) in 3 mL cuvettes for all measurements. The emission spectra were recorded at their corresponding absorption wavelengths.

Absolute quantum yield measurement. The absolute quantum yield (QY) was measured for the solid samples using a calibrated integrating sphere method with an absolute error of ±0.2%.

Powder X-ray diffraction and IR spectra. The PXRD spectra were recorded before and after grinding the samples using the Rigaku Ultima IV X-ray diffractometer. The parameters were kept constant for all samples, for example, a step width 0.2, and a scan rate of 2° min^{-1} from 5–45° (Cu, K_α radiation λ = 1.54 Å). The IR spectra were recorded using an FTIR spectrometer (FT/IR-4200, Jasco). Solid samples were mixed with KBr to obtain the spectra.

Time resolved measurements. Time-resolved fluorescence measurements were performed using a time-correlated single-photon counting (TCSPC) unit (Horiba Deltaflex). A 403 nm pulse diode laser was used, with a setup target of 10 000 counts. The solid-powder was made into a sandwich between two quartz slides and was stored in a solid-sample holder. The instrument response function was measured before the fluorescence lifetime measurements using aluminum foil. All of the decay curves were fitted using the supplied EZ Time software. All measurements were performed at room temperature (298 K). A magic angle (54.7°) configuration was used for all the measurements. All fittings were performed by maintaining the χ^2 value close to 1.

Dynamic light scattering measurements. The average particle size in the aggregated-state was measured using a Malvern particle size analyzer (zeta sizer nano-ZS), with a concentration of 10 μM.

Thermogravimetric and differential scanning calorimetry analysis. The TGA and DSC thermograms were recorded using a Themys One$^+$, Setaram instrument with a temperature range of 30–650 °C with 10 °C min^{-1} under a N_2 atmosphere.

Single crystal X-ray measurement. All measurements were performed on a Rigaku XtaLAB P200 diffractometer using multi-layer mirror monochromated Cu-Kα radiation (λ = 1.54184 Å). The data were collected at a temperature of −173 ± 1 °C to a maximum 2θ value of 149.8°. Data were collected and processed using CrysAlisPro (Rigaku Oxford Diffraction). The linear absorption coefficient, μ, for Cu-Kα radiation is 18.391 cm^{-1}. An empirical absorption correction was applied, which resulted in transmission factors ranging from 0.227 to 0.593. The data were corrected for the Lorentz and polarization effects. The structure was solved using direct methods (SIR2011)[31] and expanded using Fourier techniques. The non-hydrogen atoms were refined anisotropically. Hydrogen atoms were refined using the riding model. All calculations were performed using the Olex2 crystallographic software package except for the refinement, which was performed using SHELXL Version 2014/7.[32]

Density functional theory. The single-crystal coordination files were taken as an input file for structural optimization. The CAM-B3LYP 631-G(d,p) basis set was used to generate the output file. The HOMO and LUMO energies were calculated, and the corresponding cubes were generated using a Gaussian 09 package.

Hirshfeld surface analyses. Hirshfeld surface analysis and calculation of the void space are quantitative tools used to understand non-covalent interactions. We have generated Hirshfeld surfaces for **TMBπCBZ** and **CBZπTMB** with an iso-value of 0.5 au. The surface is generated, and the interactions are shown in terms of d_e and d_i, in which d_e and d_i are the distances of an atom external or internal to the generated Hirshfeld surfaces, together this pair (d_e and d_i) generates a 2D fingerprint plot. The different colors on the fingerprint plot represent the frequency of occurrence of the interaction. A red spot represents the direct interaction between two atoms. Ultimately it gives a normalized contact distance (d_{norm}). The d_{norm} values are mapped onto the Hirshfeld surface using a red, white, and blue color scheme; red, white, and blue regions correspond to the strong, medium, and weak interactions, respectively. All the Hirshfeld surfaces were generated using Crystal Explorer 3.1 software. The void spaces were calculated with the iso value of 0.002 a.u. within a radius of the unit cell +5 Å (default).

Synthesis and characterizations

(*E*)-9-Pentyl-3-(2-(10-(2,4,6-trimethoxyphenyl)anthracen-9-yl)vinyl)-9*H*-carbazole (TMBπCBZ). **TMOP**[17] (0.50 g, 1.01 mmol) was placed under a vacuum in a 50 mL round-bottomed two neck flask and was dissolved in dry THF (15 mL) under the continuous flow of argon gas at room temperature. Next, ^{t}BuOK (0.34 gm, 3.03 mmol) was added and stirred for 5 min. 9-Pentyl-9*H*-carbazole-3-carbaldehyde (0.30 g, 1.2 mmol) was carefully added to the solution. The reaction was allowed to stir for 3 h, and completion of the reaction was monitored using thin layer chromatography (TLC). The resulting reaction mixture was quenched with water, extracted with ethyl acetate (25 mL × 3), dried over anhydrous sodium sulphate, and concentrated under a rotary evaporator. **TMBπCBZ** was purified by column chromatography using ethyl acetate and petroleum ether (5% ethyl acetate in petroleum ether). A similar method was followed for **CBZπTMB** using diethyl ((10-(9-pentyl-9*H*-carbazol-3-yl)anthracen-9-yl) methyl)phosphonate (**CBZP**)[10] with 2,4,6-trimethoxybenzaldehyde.

TMBπCBZ. Yield 0.51 g, 85%, MP 170–172 °C. IR (ν cm^{-1}, in KBr): 3455, 3428, 3064, 2992, 2931, 2854, 2650, 2523, 1673, 1623, 1596, 1491, 1469, 1408, 1391, 1326, 1270, 1221, 1198, 1121, 1038. ^{1}H NMR (400 MHz, $CDCl_3$) δ 8.50 (d, J = 8.7 Hz, 2H), 8.37 (d, J = 1.5 Hz, 1H), 8.17 (d, J = 7.7 Hz, 1H), 7.99 (d, J = 16.5 Hz, 1H), 7.85 (dd, J = 8.5, 1.6 Hz, 1H), 7.67 (d, J = 8.4 Hz, 2H), 7.52–7.38 (m, 5H), 7.36–7.30 (m, 2H), 7.29–7.25 (m, 1H), 7.17 (d, J = 16.5 Hz, 1H), 6.40 (s, 2H), 4.34 (t, J = 7.2 Hz, 2H), 3.97 (s, 3H), 3.56 (s, 6H), 2.00–1.85 (m, 2H), 1.46–1.34 (m, 4H), 0.90 (t, J = 7.3 Hz, 3H). ^{13}C NMR (101 MHz, $CDCl_3$) δ 161.5, 159.6, 140.9, 140.4, 137.9, 133.2, 130.9, 129.9, 128.8, 127.1, 126.5, 125.9, 124.8, 124.4, 123.3, 122.9, 122.7, 120.6, 119.0, 118.7, 108.9, 108.8, 108.7, 108.6, 108.5, 91.1,

55.9, 55.5, 43.2, 29.5, 28.8, 22.5, 14.0. ESI-MS for $C_{42}H_{39}NO_3$, calc. 605.2930, found 606 $[M + 1]^+$. An X-ray structure was obtained for this sample (CCDC 2043011†).

CBZπTMB. Yield 0.41 g, 76%, MP 208–210 °C. IR (ν cm^{-1}, in KBr): 3457, 3427, 3069, 2998, 2933, 2850, 1670, 1629, 1591, 1490, 1461, 1407, 1397, 1323, 1275, 1223, 1191, 1129, 1040. ^{1}H NMR (400 MHz, $CDCl_3$) δ 8.58 (d, J = 8.7 Hz, 2H), 8.25 (d, J = 16.9 Hz, 1H), 8.16 (d, J = 1.0 Hz, 1H), 8.05 (d, J = 7.7 Hz, 1H), 7.74 (d, J = 8.6 Hz, 2H), 7.60 (d, J = 8.1 Hz, 1H), 7.55–7.46 (m, 3H), 7.43 (ddd, J = 8.8, 6.4, 1.2 Hz, 2H), 7.30 (ddd, J = 8.8, 6.3, 1.1 Hz, 2H), 7.23–7.16 (m, 2H), 6.27 (s, 2H), 4.41 (t, J = 7.3 Hz, 2H), 3.92 (s, 6H), 3.89 (s, 3H), 2.07–1.94 (m, 2H), 1.53–1.37 (m, 4H), 0.95 (t, J = 7.1 Hz, 3H). ^{13}C NMR (101 MHz, $CDCl_3$) δ 160.4, 159.7, 140.9, 139.8, 136.9, 135.6, 130.9, 129.6, 129.3, 129.1, 128.2, 127.5, 126.9, 126.8, 125.8, 124.9, 124.7, 124.6, 123.2, 122.8, 120.5, 118.9, 108.8, 108.5, 108.4, 90.9, 55.9, 55.5, 43.4, 29.6, 28.9, 22.6, 14.1. ESI-MS for $C_{42}H_{39}NO_3$, calc. 605.2930, found 606 $[M + 1]^+$. An X-ray structure was obtained for this sample (CCDC 2043012†).

Conclusions

In conclusion, two easily affordable positional isomeric AIEgens **TMBπCBZ** and **CBZπTMB** are presented by interchanging the two electron-rich **CBZ** and **TMB** cores. Both of these isomers are highly emissive in the solid-state, but unexpectedly, only **TMBπCBZ** exhibits reversible high-contrast PFC-features, not **CBZπTMB**. This dissimilarity was interpreted using SCXRD, PXRD, DSC, and fluorescence lifetime studies. Multiple weak C···H interactions, along with the formation of cavities (validated by crystal packing and Hirshfeld surface analyses studies), are beneficial for the fluorescence switching of **TMBπCBZ** upon grinding or applying pressure. Notably, twisted conformational structures of these molecules play a crucial role in their strong emission in the solid-state. In contrast, twisted **CBZπTMB** possesses a strong intramolecular interaction that enforces the planarity of the system, gaining significant stability with a six-membered ring in this molecular conformation. This coplanarity effect for the twisted **CBZπTMB** AIEgen seems to be detrimental to the exhibition of PFC-features. Thus, this work has delivered a novel concept on the cause of inactive PFC behavior in a twisted π-conjugated system. Along with many other established design strategies, this concept could enable the development of high contrast PFC-active materials. The practical applications of a multiply reversible security writing device proves the efficacy of this π-conjugate.

Conflicts of interest

There are no conflicts to declare.

Acknowledgements

We thank DST-SERB (CRG/2018/000456) for financial support. BP thanks BITS-Pilani Hyderabad for his fellowship and the use of the NMR/X-ray facilities.

Notes and references

1 Y. Wang, W. Leu, L. Ren and G. Ge, *Mater. Chem. Front.*, 2019, **3**, 1661–1670.
2 Y. Gong, Y. Zhang, W. Z. Yuan, J. Z. Sun and Y. Zhang, *J. Phys. Chem. C*, 2014, **118**, 10998–11005.
3 Y. Hou, J. Du, J. Hou, P. Shi, K. Wang, S. Zhang, T. Han and Z. Li, *Dyes Pigm.*, 2019, **160**, 830–838.
4 C. Ge, Y. Liu, X. Ye, X. Zheng, Q. Han, J. Liu and X. Tao, *Mater. Chem. Front.*, 2017, **1**, 530–537.
5 L. Huang, X. Wen, J. Liu, M. Chen, Z. Ma and X. Jia, *Mater. Chem. Front.*, 2019, **3**, 2151–2156.
6 G. Huang, Y. Jiang, J. Wang, Z. Li, B. S. Li and B. Z. Tang, *J. Mater. Chem. C*, 2019, **7**, 12709.
7 H. Zhu, S. Weng, H. Zhang, H. Yu, L. Kong, Y. Zhong, Y. Tian and J. Yang, *CrystEngComm*, 2018, **20**, 2772–2779.
8 Q. Yang, D. Li, W. Chi, R. Guo, B. Yan, J. Lan, X. Liu and J. Yin, *J. Mater. Chem. C*, 2019, **7**, 8244–8249.
9 (*a*) H. J. Kim, J. Gierschner and S. Y. Park, *J. Mater. Chem. C*, 2020, **8**, 7417–7421; (*b*) B. K. An, D. S. Lee, J. S. Lee, Y. S. Park, H. S. Song and S. Y. Park, *J. Am. Chem. Soc.*, 2004, **126**, 10232–10233; (*c*) J. W. Chen, B. Xu, X. Y. Ouyang, B. Z. Tang and Y. Cao, *J. Phys. Chem. A*, 2004, **108**, 7522–7526; (*d*) F. Wang, M. Y. Han, K. Y. Mya, Y. Wang and Y. H. Lai, *J. Am. Chem. Soc.*, 2005, **127**, 10350–10355; (*e*) B. J. Xu, Z. G. Chi, H. Y. Li, X. Q. Zhang, X. F. Li, S. W. Liu, Y. Zhang and J. R. Xu, *J. Phys. Chem. C*, 2011, **115**, 17574–17581; (*f*) B. J. Xu, Z. G. Chi, X. F. Li, H. Y. Li, W. Zhou, X. Q. Zhang, C. C. Wang, Y. Zhang, S. W. Liu and J. R. Xu, *J. Fluoresc.*, 2011, **21**, 433–441.
10 B. Prusti and M. Chakravarty, *ACS Omega*, 2019, **4**, 16963–16971.
11 (*a*) Y. Ooyama, T. Sugiyama, Y. Oda, Y. Hagiwara, N. Yamaguchi, E. Miyazaki, H. Fukuoka, T. Mizumo, Y. Harima and J. Ohshita, *Eur. J. Org. Chem.*, 2012, 4853–4859; (*b*) H. Y. Li, X. Q. Zhang, Z. G. Chi, B. J. Xu, W. Zhou, S. W. Liu, Y. Zhang and J. R. Xu, *Org. Lett.*, 2011, **13**, 556–559.
12 Y. Zhan, P. Gong, P. Yang, Z. Jin, Y. Bao, Y. Li and Y. Xu, *RSC Adv.*, 2016, **6**, 32697–32704.
13 Y. Lin, T. B. Kouznetsova and S. L. Craig, *J. Am. Chem. Soc.*, 2020, **142**, 99–103.
14 X. Q. Zhang, Z. G. Chi, X. Zhou, S. W. Liu, Y. Zhang and J. R. Xu, *J. Phys. Chem. C*, 2012, **116**, 23629–23638.
15 X. Zhou, H. Y. Li, Z. G. Chi, X. Q. Zhang, J. Y. Zhang, B. J. Xu, Y. Zhang, S. W. Liu and J. R. Xu, *New J. Chem.*, 2012, **36**, 685–693.
16 Y. L. Wang, W. Liu, L. Y. Bu, J. F. Li, M. Zheng, D. T. Zhang, M. X. Sun, Y. Tao, S. F. Xue and W. J. Yang, *J. Mater. Chem. C*, 2013, **1**, 856–862.
17 K. Mandal, D. Jana, B. K. Ghorai and N. R. Jana, *ACS Appl. Nano Mater.*, 2019, **2**, 3292–3299.
18 (*a*) B. Prusti, H. Aggarwal and M. Chakravarty, *ChemPhotoChem*, 2020, **4**, 347–356; (*b*) B. Prusti and M. Chakravarty, *Analyst*, 2020, **145**, 1687–1694; (*c*) M. Z. K. Baig, B. Prusti and M. Chakravarty, *J. Mater. Chem. C*, 2019, **7**, 3735–3739;

(*d*) B. Prusti and M. Chakravarty, *Dyes Pigm.*, 2020, **181**, 108543.

19 Y. J. Cheng, J. S. Wu, P. I. Shih, C. Y. Chang, P. C. Jwo, W. S. Kao and C. S. Hsu, *Chem. Mater.*, 2011, **23**, 2361–2369.

20 (*a*) Y. Hong, J. W. Y. Lam and B. Z. Tang, *Chem. Soc. Rev.*, 2011, **40**, 5361–5388; (*b*) Y. Chen, J. W. Y. Lam, R. T. K. Kwok, B. Liu and B. Z. Tang, *Mater. Horiz.*, 2019, **6**, 428–433; (*c*) L. Li, H. Nie, M. Chen, J. Sun, A. Qin and B. Z. Tang, *Faraday Discuss.*, 2017, **196**, 245–253.

21 N. Zhang, H. Chen, Y. Fan, L. Zhou, S. Trepout, J. Guo and M. H. Li, *ACS Nano*, 2018, **12**, 4025–4035.

22 B. Fang, M. Chu, Z. Wu, Y. Shi, Y. S. Zhao and M. Yin, *J. Mater. Chem. C*, 2019, **7**, 4434–4440.

23 B. Roy, M. C. Reddy and P. Hazra, *Chem. Sci.*, 2018, **9**, 3592–3606.

24 J. Wu, Y. Cheng, J. Lan, D. wu, S. Qian, L. Yan, Z. He, X. Li, K. Wang, B. Zou and J. You, *J. Am. Chem. Soc.*, 2016, **138**, 12803.

25 (*a*) Y. Matsuo, Y. Wang, H. Ueno, T. Nakagawa and H. Okada, *Angew. Chem., Int. Ed.*, 2019, **58**, 8762–8767; (*b*) *Mechanochromic fluorescent materials phenomena, materials and applications*, ed. J. Xu and Z. Chi, Royal Society of Chemistry, 2014, p. 167; (*c*) Y. Ren and T. Baumgartner, *Inorg. Chem.*, 2012, **51**, 2669–2678.

26 M. Ikeya, G. Katada and S. Ito, *Chem. Commun.*, 2019, **55**, 12296–12299.

27 W. Yang, Y. Yang, Y. Qiu, X. Cao, Z. Huang, S. Gong and C. Yang, *Mater. Chem. Front.*, 2020, **4**, 2047–2053.

28 Y. Li, Z. Ma, A. Li, W. Xu, Y. Wang, H. Jiang, K. Wang, Y. Zhao and X. Jia, *ACS Appl. Mater. Interfaces*, 2017, **9**, 8910–8918.

29 A. R. Sheth, J. W. Lubach, E. J. Munson, F. X. Muller and D. J. W. Grant, *J. Am. Chem. Soc.*, 2005, **127**, 6641–6651.

30 (*a*) P. Shi, D. Deng, C. He, L. Ji, Y. Duan, T. Han, B. Suo and W. Zou, *Dyes Pigm.*, 2020, **173**, 107884; (*b*) P. Z. Chen, J. X. Wang, L. Y. Niu, Y. Z. Chen and Q. Z. Yang, *J. Mater. Chem. C*, 2017, **5**, 12538.

31 M. C. Burla, R. Caliandro, M. Camalli, B. Carrozzini, G. L. Cascarano, C. Giacovazzo, M. Mallamo, A. Mazzone, G. Polidori and R. Spagna, *J. Appl. Crystallogr.*, 2012, **45**, 357.

32 G. M. Sheldrick, *Acta Crystallogr., Sect. A: Found. Crystallogr.*, 2008, **64**, 112.